



Optical follow-up of the neutron star–black hole mergers S200105ae and S200115j

Shreya Anand^{1,30}✉, Michael W. Coughlin^{1,2,30}✉, Mansi M. Kasliwal¹, Mattia Bulla³, Tomás Ahumada⁴, Ana Sagués Carracedo⁵, Mouza Almualla⁶, Igor Andreoni¹, Robert Stein^{7,8}, Francois Foucart⁹, Leo P. Singer^{10,11}, Jesper Sollerman¹², Eric C. Bellm¹³, Bryce Bolin¹, M. D. Caballero-García¹⁴, Alberto J. Castro-Tirado^{15,16}, S. Bradley Cenko^{10,11}, Kishalay De¹, Richard G. Dekany¹⁷, Dmitry A. Duvvuri¹, Michael Feeney¹⁷, Christoffer Fremling¹, Daniel A. Goldstein¹, V. Zach Golkhou^{13,18}, Matthew J. Graham¹, Nidhal Guessoum⁶, Matthew J. Hankins¹, Youdong Hu^{15,19}, Albert K. H. Kong^{10,20}, Erik C. Kool¹², S. R. Kulkarni¹, Harsh Kumar²¹, Russ R. Laher²², Frank J. Masci²², Przemek Mróz¹, Samaya Nissanke²³, Michael Porter¹⁷, Simeon Reusch^{7,8}, Reed Riddle¹⁷, Philippe Rosnet²⁴, Ben Rusholme²², Eugene Serabyn²⁵, R. Sánchez-Ramírez²⁶, Mickael Rigault²⁴, David L. Shupe²², Roger Smith¹⁷, Maayane T. Soumagnac^{1,2,27,28}, Richard Walters¹⁷ and Azamat F. Valeev^{1,3,29}

LIGO and Virgo's third observing run revealed the first neutron star–black hole (NSBH) merger candidates in gravitational waves. These events are predicted to synthesize r-process elements^{1,2} creating optical/near-infrared 'kilonova' emission. The joint gravitational wave and electromagnetic detection of an NSBH merger could be used to constrain the equation of state of dense nuclear matter³, and independently measure the local expansion rate of the Universe⁴. Here, we present the optical follow-up and analysis of two of the only three high-significance NSBH merger candidates detected to date, S200105ae and S200115j, with the Zwicky Transient Facility⁵. The Zwicky Transient Facility observed ~48% of S200105ae and ~22% of S200115j's localization probabilities, with observations sensitive to kilonovae brighter than -17.5 mag fading at 0.5 mag d^{-1} in the g- and r-bands; extensive searches and systematic follow-up of candidates did not yield a viable counterpart. We present state-of-the-art kilonova models tailored to NSBH systems that place constraints on the

ejecta properties of these NSBH mergers. We show that with observed depths of apparent magnitude ~ 22 mag, attainable in metre-class, wide-field-of-view survey instruments, strong constraints on ejecta mass are possible, with the potential to rule out low mass ratios, high black hole spins and large neutron star radii.

During the third observing run (O3), LIGO and Virgo detected eight neutron star–black hole (NSBH) and six binary neutron star (BNS) candidate events at various confidence levels, with localization regions spanning a few tens to several thousands of square degrees and median distances in the range ~ 108 – 630 Mpc. We do not include S190718a as a BNS merger candidate due to glitches in the detectors near trigger time, which have a very high terrestrial probability ($>98\%$). All of the NSBH candidates had $\sim 100\%$ probability of one of the component masses being $<3 M_{\odot}$, and are therefore likely to be neutron stars. Only two candidates, S200105ae (ref. ⁶) and S200115j (ref. ⁷), initially had finite probability of leaving behind a non-zero amount of neutron star material outside the final

¹Division of Physics, Mathematics, and Astronomy, California Institute of Technology, Pasadena, CA, USA. ²School of Physics and Astronomy, University of Minnesota, Minneapolis, MN, USA. ³Nordita, KTH Royal Institute of Technology and Stockholm University, Stockholm, Sweden. ⁴Department of Astronomy, University of Maryland, College Park, MD, USA. ⁵The Oskar Klein Centre, Department of Physics, Stockholm University, Stockholm, Sweden. ⁶Physics Department, American University of Sharjah, Sharjah, United Arab Emirates. ⁷Deutsches Elektronen Synchrotron DESY, Zeuthen, Germany. ⁸Institut für Physik, Humboldt-Universität zu Berlin, Berlin, Germany. ⁹Department of Physics, University of New Hampshire, Durham, NH, USA. ¹⁰Astrophysics Science Division, NASA Goddard Space Flight Center, Greenbelt, MD, USA. ¹¹Joint Space-Science Institute, University of Maryland, College Park, MD, USA. ¹²The Oskar Klein Centre, Department of Astronomy, Stockholm University, Stockholm, Sweden. ¹³DIRAC Institute, Department of Astronomy, University of Washington, Seattle, WA, USA. ¹⁴Astronomical Institute of the Academy of Sciences, Prague, Czech Republic. ¹⁵Instituto de Astrofísica de Andalucía (IAA-CSIC), Granada, Spain. ¹⁶Departamento de Ingeniería de Sistemas y Automática, Escuela de Ingenieros Industriales, Universidad de Málaga, Unidad Asociada al CSIC, Málaga, Spain. ¹⁷Caltech Optical Observatories, California Institute of Technology, Pasadena, CA, USA. ¹⁸The eScience Institute, University of Washington, Seattle, WA, USA. ¹⁹Facultad de Ciencias Campus, Universidad de Granada, Granada, Spain. ²⁰Institute of Astronomy, National Tsing Hua University, Hsinchu, Taiwan. ²¹Indian Institute of Technology Bombay, Mumbai, India. ²²IPAC, California Institute of Technology, Pasadena, CA, USA. ²³Center of Excellence in Gravitation and Astroparticle Physics, University of Amsterdam, Amsterdam, the Netherlands. ²⁴Laboratoire de Physique de Clermont, Université Clermont Auvergne, CNRS/IN2P3, Clermont-Ferrand, France. ²⁵Jet Propulsion Laboratory, California Institute of Technology, Pasadena, CA, USA. ²⁶INAF-Instituto di Astrofisica e Planetologia Spaziali, Rome, Italy. ²⁷Lawrence Berkeley National Laboratory, Berkeley, CA, USA. ²⁸Department of Particle Physics and Astrophysics, Weizmann Institute of Science, Rehovot, Israel. ²⁹Special Astrophysical Observatory, Russian Academy of Sciences, Nizhny Arkhyz, Russia. ³⁰These authors contributed equally: Shreya Anand, Michael W. Coughlin.

✉e-mail: sanand@caltech.edu; cough052@umn.edu

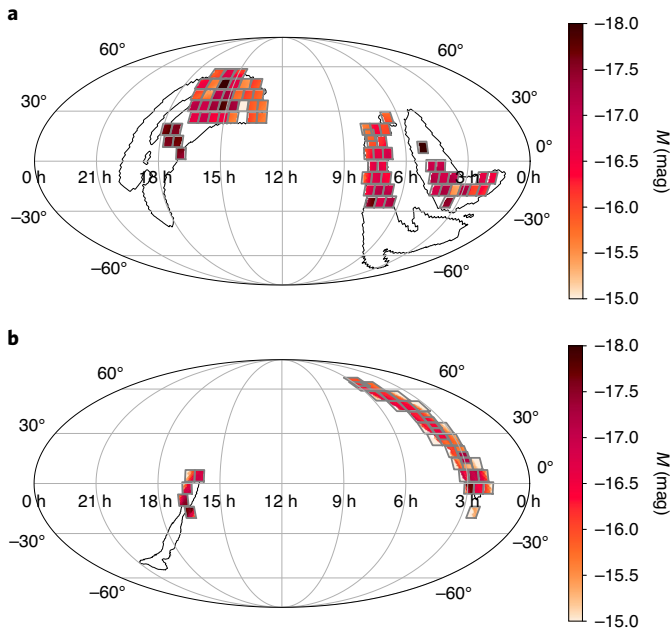


Fig. 1 | Absolute magnitudes corresponding to ZTF pointings in the skymap. a, b. The absolute magnitudes that correspond to the distance provided in the GW LALInference skymap, measured at the centre of each field, and the deepest limiting magnitude in either *g*- or *r*-bands (computed as a median over the CCDs (charge-coupled devices) in a particular field) for S200105ae (**a**) and S200115j (**b**). The 90% probability region contours are shown as a guide to the eye.

black hole, although updated analysis⁸ of S200115j gives a >99% probability of leaving behind a remnant. S200105ae⁶ and S200115j⁷ were both detected in January, at 5 January 2020 16:24:26 and 15 January 2020 04:23:09 UTC, respectively (see Methods). During O3, the Zwicky Transient Facility (ZTF) ran a dedicated follow-up programme to identify optical counterparts to gravitational wave (GW) candidates (for example, refs. 9–11). Together with the Global Relay of Observatories Watching Transients Happen (GROWTH) network (<http://growth.caltech.edu/>), ZTF rapidly followed up and classified objects that were consistent with the candidates. Over the three nights following detection, ZTF covered 3,300 deg² and 1,100 deg² for S200105ae and S200115j, respectively, corresponding to ~52% of the localization probability for S200105ae, and ~22% of the localization probability for S200115j (see Methods). S200115j occurred during Palomar night-time, so our triggered observations began immediately, but poor weather on the two nights following the merger prevented further follow-up observations.

As a metric for understanding the efficacy of ZTF's observations, we show the mean absolute magnitude to which we are sensitive as a function of sky location in Fig. 1. This uses the median distance at each point on the skymap and compares with our median limiting magnitude in each of the fields (see Extended Data Fig. 1). The best limiting magnitudes correspond to absolute magnitudes $M \lesssim -16$ mag for both events, with typical observations ranging from $M \approx -16.5$ mag to $M \approx -17.5$ mag. AT2017gfo (ref. 12), the optical counterpart of GW170817, peaked at $M \approx -16$ mag, and kilonovae (KNe) from NSBH models are typically brighter than those from BNSs^{13–15}, meaning that our observations are in the magnitude range required for detection.

In addition to requiring multi-epoch coverage of large localizations at sufficient depth, these searches normally yield hundreds of thousands of alerts that require quick and thorough vetting (see

Methods for specific criteria and Extended Data Fig. 2). We successfully narrowed this list down to a select few candidates consistent with our criteria within minutes for both events; only 22 candidates for S200105ae and 6 candidates of S200115j remained (see Methods for the selection criteria). GROWTH obtained follow-up photometry and spectroscopy for the candidates meeting our requirements to assess their relation to either event. Using a global array of telescopes (see Methods for observatories and instruments), we reject each of our candidates on the basis of the following criteria:

- Spectroscopic classification: candidates spectroscopically determined to be supernovae (SNe) or other transients (see Fig. 2 and Supplementary Fig. 4).
- Slow photometric evolution: candidates evolving at $<|0.3|$ mag per day, below the expected fast evolution for KNe over the course of a week (see Methods and Supplementary Fig. 2 for justification and Supplementary Fig. 1 for candidate light curves).
- Stellar variables: candidates coincident with point sources, likely to be variable stars or cataclysmic variables in the Milky Way.
- Slow-moving asteroids: candidates that are later determined to be asteroids or other Solar System objects (see Supplementary Fig. 3).

After thorough vetting, we found no candidate remaining that could plausibly be associated with either event (see the candidates' spatial distribution in Extended Data Fig. 3 and the lists of the candidates in Supplementary Tables 2–4).

The non-detection in our searches allows us to impose both empirical and model-based constraints on photometric evolution for a counterpart falling within the observed region. To place the coverage and limits in context, we compare our observations to empirical models of evolution with a linear rise and decay (Fig. 3) and KN models that allow ejecta masses to vary (Fig. 4). Using simulation¹⁶ to inject and recover simulated KNe, we show in Fig. 3 that ZTF should have detected a KN in the observed region of either skymap brighter than $M \lesssim -17.5$ mag and fading slower than 0.5 mag per day in both the *g*- and *r*-bands. We simulate KNe with various absolute magnitudes and evolution rates assuming no colour evolution. Our recovery criteria require a single KN detection in either filter. We plot the absolute magnitudes of the KNe at peak along with their evolution rates. We also mark AT2017gfo, which had a peak absolute magnitude of about -16 mag in the optical bands, fading at ~ 0.5 mag per day in the *g*- and *r*-bands. The lack of observations on the first night for S200105ae, owing to a delay in the release of the initial skymap, weakened constraints compared with S200115j (see Methods). We note here that our sensitivity to rising or fading KNe is highly dependent on latency in starting observations and number of follow-up epochs.

For our model-dependent constraints, assuming that the KN is in the area observed, we take a series of representative median magnitudes for each night of observations and compare them to light curve models from the radiative transfer code POSSIS¹⁷; we generated them using a new grid of KN spectra tailored to NSBH mergers. These are summarized in Fig. 4, where we show light curves that are allowed (grey) or ruled out at different distances (light to dark blue) by the median magnitudes achieved with our observations of S200105ae and S200115j (see Methods). We find that the median magnitudes place weak constraints on these models. Specifically, all KN light curves that we consider are fainter than the limits for S200105ae, whereas only a few models with large amounts of post-merger ejecta ($\geq 0.05 M_{\odot}$) are ruled out for S200115j at polar viewing angles and for the nearest-by portions of the skymap. We also note that due to our coverage in both sky-maps being less than 50%, our model constraints for S200105ae and S200115j apply only within the observed region. For comparison, Fig. 4c shows NSBH models from our new grid that are ruled out

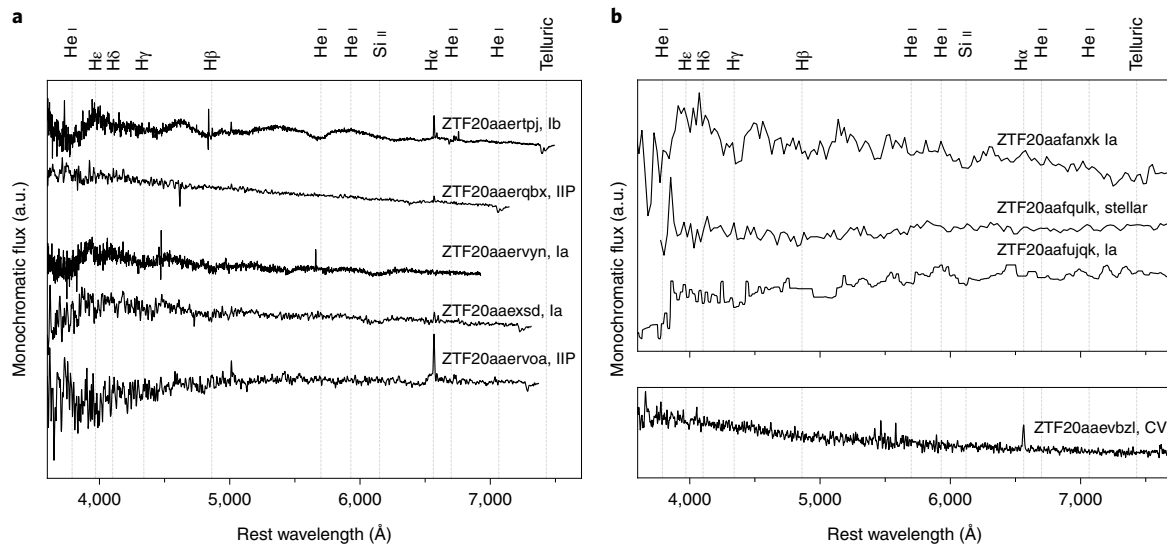


Fig. 2 | Spectra of all of the candidates ruled out spectroscopically during both campaigns. To visualize all of the spectra on the same figure, we have applied a vertical offset to the flux and plotted each spectrum at the mean signal-to-noise ratio. The vertical dashed lines correspond to common spectral absorption and emission features in SN spectra. **a**, Spectra of five S200105ae candidates taken with the Optical System for Imaging and low Resolution Integrated Spectroscopy (OSIRIS) on the Gran Telescopio Canarias (GTC) of the Roque de los Muchachos Observatory in La Palma, Spain^{25,26}. The top three spectra were taken on 11 January, and the bottom two were taken on 10 January. From top to bottom, ZTF20aaertpj was classified as a SN Ib at $z(s)=0.026$, where $z(s)$ indicates a spectroscopic redshift, ZTF20aaerqbx was classified as a SN IIP at $z(s)=0.098$, ZTF20aaervyn was shown to be a SN Ia at $z(s)=0.112$, ZTF20aaerxsd is a SN Ia at $z(s)=0.055$, and ZTF20aaervoav was classified as a SN IIP at $z(s)=0.046$. **b**, Top: all spectra taken with the SED Machine (SEDM) on the Palomar 60-inch telescope (P60); from top to bottom, ZTF20aafanxk (S200105ae) was classified as a SN Ia at $z(s)=0.103$ on 18 January, the spectrum of ZTF20aafquik (S200115j), observed on 24 January, indicates that it is likely to be stellar, and ZTF20aafujqk (S200105ae), also observed on 18 January, was classified as a SN Ia at $z(s)=0.074$. Bottom: the spectrum of ZTF20aaevbzl (S200105ae) taken by the Double Spectrograph (DBSP) on the Palomar 200-inch telescope (P200), obtained on 18 January 2020, contains a $H\alpha$ feature in a mostly featureless blue continuum that is indicative of it being a cataclysmic variable (CV).

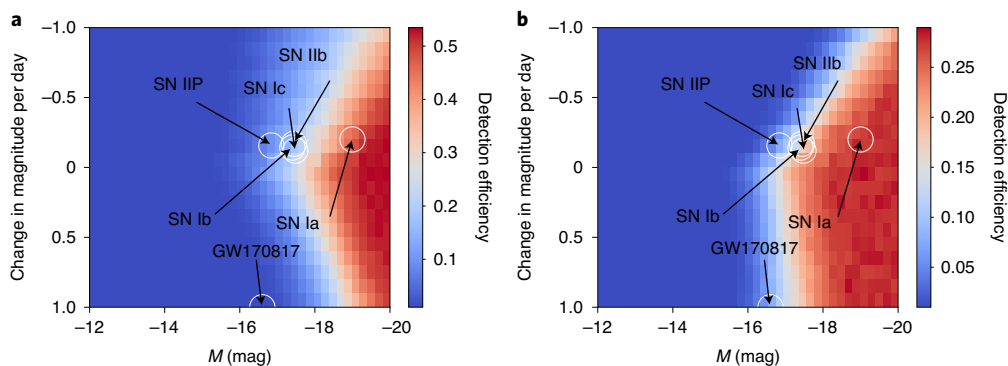


Fig. 3 | Detection efficiency of simulated KNe based on ZTF observations. **a, b**, The ratio of recovered versus injected KNe (efficiency) identified in observations in a skymap for an analytic model varying absolute magnitude and change in magnitude per day for S200105ae (**a**) and S200115j (**b**) in both the g - and r -bands. Here, the magnitude corresponds to the peak absolute magnitude of the injected KNe for a linear model with a given rise or decay rate. The maximum of the colour scales is set to the maximum efficiency achieved (at $M=-20$ mag), which was 53% for S200105ae and 29% for S200115j. The approximate peak absolute magnitudes and approximate rise rates for some common SNe types are also plotted. The absolute magnitude at detection and the approximate decline rate of GW170817 are shown as a guide to the eye.

by the DECam observations of S190814bv¹⁸; such limits are more robust than our limits on S200105ae and S200115j due to DECam covering 98% of the skymap (compared with 48% and 22%). For that well-localized event, the deeper DECam limits and the closer distance for S190814bv ($d=267 \pm 52$ Mpc; ref.¹¹) lead to a larger number of models ruled out.

To understand the scientific performance and potential of metre-class, wide-field-of-view imagers as powerful tools in electromagnetic searches for GW counterparts follow-up, we determine

what constraints are possible on the viewing angle (θ_{obs}) of a potential counterpart, the dynamical ($M_{\text{ej,dyn}}$) and post-merger ($M_{\text{ej,pm}}$) ejecta and the binary parameters with the deepest ZTF exposures on each night (see Methods). For S200105ae, with 5 min exposures reaching a depth of $m_{\text{AB}} \geq 22$ mag, ZTF would be sensitive to a large fraction of KNe with polar and intermediate viewing angles. Non-detection of a KN in these circumstances could rule out $M_{\text{ej,dyn}} \leq 0.02 M_{\odot}$ and $M_{\text{ej,pm}} \leq 0.04 M_{\odot}$ for polar directions at 283 Mpc (see Extended Data Fig. 4). Using these $M_{\text{ej}}-\theta_{\text{obs}}$ constraints, we could estimate the

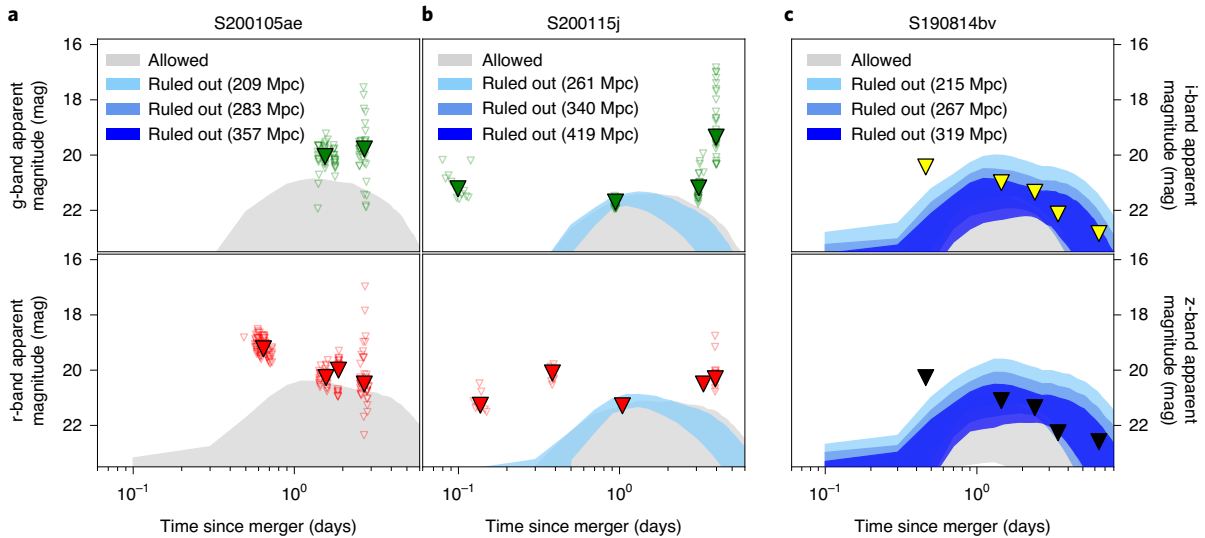


Fig. 4 | Constraints on KN model parameters based on median limiting magnitudes. **a–c**, All KN light curves ruled out by median 5σ limits on S200105ae (ZTF) **(a)**, S200115j (ZTF) **(b)** and S190814bv (DECAM) **(c)**. For S200105ae and S200115j, median apparent magnitudes, with g-band in the top panels and r-band in the bottom panels, are shown with filled triangles, whereas individual limits are shown with empty triangles. Limits shown for S190814bv are median depth values from table 1 of ref. ¹⁸, with i-band in the top panel and z-band in the bottom panel. KN light curves are calculated with POSSIS¹⁷; we show in blue when they are ruled out by the limits at three different distances (corresponding to median distances and $\pm 1\sigma$ distance uncertainties from LIGO) and in grey otherwise. For each distance, the shaded area represents the range spanned by different models and different viewing angles (with the brighter end generally corresponding to higher masses and polar orientations and the fainter end to lower masses and equatorial orientations). The median limits for S200105ae do not constrain any KN models for any distance assumptions, whereas for S200115j they place constraints only on the models for nearby KNe (light blue). For S190814bv, median limits constrain KN models for all distance assumptions.

maximum aligned spin of the black hole component for different assumptions of the viewing angle, binary mass ratio and neutron star radius. Non-detection would further rule out low mass ratios, high black hole spins and/or large neutron star radii (see Extended Data Fig. 5). For high mass ratios, the limit on $M_{\text{ej,dyn}}$ would provide tighter constraints than the limit on $M_{\text{ej,pm}}$. As $M_{\text{ej,dyn}}$ is reasonably well known from simulations¹⁹, our modelling of the ejected mass is not an important source of uncertainty. For low mass ratios, the limit on $M_{\text{ej,pm}}$ would provide tighter constraints. Current simulations only allow us to constrain $M_{\text{ej,pm}}$ to within a factor of 2–3 (ref. ²⁰), and are in this case an important source of modelling uncertainty. Here, we derive an upper limit on the black hole spin using a conservative estimate of $M_{\text{ej,pm}}$. Improved simulations that provide better estimates of $M_{\text{ej,pm}}$ could make these limits tighter in the future (see Extended Data Fig. 6 for the binary parameter region not constrained by our simulations).

The available parameter space could also be substantially reduced if we knew the chirp mass of the binary¹⁴, which is not yet published by LIGO-Virgo. For S200115j, whose median distance was ~ 60 Mpc greater than S200105ae, the deepest exposures would only be sensitive to KNe at short distances, and thus place weak constraints on the binary parameters.

Revisiting the follow-ups of S190814bv with the updated NSBH grid, we find more stringent constraints on the ejecta mass and binary parameters than for S200105ae, even using median observations (Fig. 4). Polar orientations are ruled out at distances ≤ 267 Mpc, limiting the ejecta masses to $M_{\text{ej,dyn}} \lesssim 0.01 M_{\odot}$ and $M_{\text{ej,pm}} \lesssim 0.01 M_{\odot}$. At intermediate orientations ($46^{\circ} \lesssim \theta_{\text{obs}} \lesssim 53^{\circ}$), these constraints are $M_{\text{ej,dyn}} \lesssim 0.02 M_{\odot}$ and $M_{\text{ej,pm}} \lesssim 0.03 M_{\odot}$ (see Extended Data Fig. 4). We also find that deep i- and z-band exposures contribute significantly towards constraining a larger portion of the $M_{\text{ej}}-\theta_{\text{obs}}$ and binary parameter space (see Extended Data Fig. 7). The literature on KN models^{15,21} has predicted KNe from NSBH mergers to be brighter in the i- and z-bands compared with the g- and r-bands. The same reddened emission

is evident in our models (see Extended Data Figs. 8 and 9), and is demonstrated by our reanalysis of the DECAM upper limits on S190814bv. Thus observations in redder bands will yield better overall constraints on NSBH KN emission.

Several works in the literature^{13–15} have shown that KNe from NSBH mergers are generally brighter than those resulting from BNS mergers. A similar behaviour is found in NSBH and BNS models computed here and in ref. ²², respectively. Although the comparison is sensitive to the specific binary properties and thus ejecta masses adopted, we identify some general behaviours using typical values from analytical models calibrated to numerical simulations^{19,23} (for example, for a $1.2\text{--}1.4 M_{\odot}$ BNS merger with $R = 12$ km: $M_{\text{ej,dyn}}^{\text{BNS}} = 0.005 M_{\odot}$, $M_{\text{ej,pm}}^{\text{BNS}} = 0.05 M_{\odot}$; for a $1.2\text{--}6 M_{\odot}$ NSBH merger with black hole spin of 0.75: $M_{\text{ej,dyn}}^{\text{NSBH}} = 0.05 M_{\odot}$ and $M_{\text{ej,pm}}^{\text{NSBH}} = 0.05 M_{\odot}$). At peak, the difference in brightness between NSBH and BNS mergers is relatively small in both the g- and r-bands. The evolution after peak, however, is very different between the two systems. Compared with BNS mergers, NSBH mergers produce approximately ten times more massive dynamical ejecta and are thus associated with longer diffusion timescales, as photons take longer to diffuse out of the high-density and lanthanide-rich dynamical ejecta. Consequently, KNe from NSBH mergers evolve more slowly after peak and therefore stay bright longer than those resulting from BNS mergers. The difference can be as large as $\Delta m \approx 2$ mag about three days post-peak for favourable viewing angles. The different evolution post-peak explains why constraints derived above for S190814bv are tighter than those determined using BNS models¹⁸. The slower evolution of NSBH compared with BNS mergers makes the former promising candidates for future follow-up studies. This slower evolution is fairly robust to the choice of parameters as long as the neutron star is disrupted by its black hole companion.

Looking forward, achieving increased and consistent depth over our observations and supplementing r- and g-band observations with an i-band observation will be key to increasing our chances of finding a KN and/or discerning properties of the merger (see Methods).

NSBH binaries, with a combination of intrinsically longer-lasting emission, higher signal-to-noise ratios and therefore smaller sky areas (sky area $\approx \frac{1}{\text{SNR}^2}$), as well as high rates based on the three high-significance NSBH candidates observed during O3, makes them ideal for counterpart searches, which are important for measuring the Hubble constant given their improved inclination measurements over BNS counterparts²⁴. Furthermore, the uncertainty in the time delay between a merger and its peak light curve motivates obtaining observations one night after the merger; the most constraining limits from our analysis correspond to one night post-merger, when the KN is brightest (see Fig. 4). Although low-latency follow-up is crucial for determining whether an early-time lanthanide-free component is present in these KNe, observations one night after are equally important for detection or application of ejecta mass constraints. In this work, we have demonstrated a methodology for deriving strong constraints on NSBH KN models even in the case of non-detection of a counterpart, and demonstrated that such valuable constraints are within reach of wide-field-of-view, metre-class imagers.

To close, we highlight the immense promise of undertaking searches for the KN counterparts of NSBH mergers. The dearth of electromagnetic observations of NSBH systems compared with BNS systems (discovered in X-ray binaries), and the difficulty of distinguishing between a low-mass BBH and an NSBH system from the GWs points to the ‘smoking gun’ nature of KNe in confirming the existence of such systems. Kilonovae are among the most valuable probes of the empirical ‘mass gap’ between the stellar mass neutron star and black hole systems, and will allow us to observationally confirm the correlation between the mass ratio of the binary and the fate of the remnant, even in the case of non-detection. These could be jointly addressed by GW and electromagnetic facilities that possess a combination of large fields-of-view and deep sensitivity. Continuing follow-ups of NSBH mergers are essential to provide key insights into the nature of the elusive NSBH population as a whole.

Methods

GW candidates. LIGO/Virgo S200105ae⁶, a candidate NSBH event which occurred at 5 January 2020 16:24:26.057 UTC, was discovered by the Advanced LIGO-Livingston detector, with Virgo also observing at the time. The event was initially reported as having 97% terrestrial probability, with a false alarm rate (FAR) of 24 per year, and therefore not generally of interest for follow-up. However, the LIGO and Virgo collaborations reported that the false alarm rate was probably grossly overestimated as a single-instrument event, and the presence of a chirp-like structure in the spectrograms gave confidence in it being a real event^{6,27}. Unlike other NSBH events, this trigger initially had remnant probability $p_{\text{remnant}} > 0\%$; this parameter indicates the probability of remnant matter existing outside the merger that could generate an electromagnetic transient counterpart^{19,28}. Similar to GW190425²⁹, as a single-detector event, the 90% credible region spans 7,720 deg², with an all-sky averaged distance to the source of 265 ± 81 Mpc. After our observations on the three following nights were complete, a new LALInference skymap was released³⁰. The LALInference map slightly reduced the 90% area to 7,373 deg² (while making the 50% area larger), modified the all-sky averaged distance to the source to 283 ± 74 Mpc and shifted more of the probability to be uniform across the lobes (including the one near the Sun, which was at ~ 19 h in RA and approximately -22° in declination at the time of the trigger, see Extended Data Fig. 3). Further parameter estimation confirmed that the merger was likely to have contained one object with component masses $< 3 M_{\odot}$, and therefore likely to be a neutron star ($> 98\%$ probability), but considerably reduced the estimated remnant probability ($p_{\text{remnant}} < 1\%$).

LIGO/Virgo S200115j⁷, a candidate NSBH event that occurred at 15 January 2020 04:23:09.742 UTC, was discovered by the two Advanced LIGO interferometers and the Advanced Virgo interferometer. This event was classified as a MassGap event, with HasNS $> 99\%$, indicating that one component’s mass fell into the range between 3 and $5 M_{\odot}$, and the other component was $< 3 M_{\odot}$, and therefore likely to be a neutron star, respectively. Although S200115j initially had a non-zero terrestrial probability, its revised classification reflected that the trigger was astrophysical (MassGap $> 99\%$), with a FAR of 1 per 1,513 years. As a three-detector localized event, the skymap was better constrained than for S200105ae, spanning 908 deg² (at 90% confidence). It also contained two disjointed lobes, one in each hemisphere, and had a median distance of 331 ± 97 Mpc. Considering all of these factors, along with $p_{\text{remnant}} = 8.7\%$, we chose to trigger

our programme for ZTF follow-up and obtained target-of-opportunity (TOO) observations. Nearly three days later, an updated LALInference skymap reduced the 90% credible region to 765 deg² and shifted most of the probability to the southernmost tip of the lower lobe⁸, see Extended Data Fig. 3. The median distance was only slightly modified to 340 ± 79 Mpc. This update also distinguished S200115j from other NSBH candidates as an exceptional event for electromagnetic follow-up, with $p_{\text{remnant}} > 99\%$ (ref.⁹).

Observing plan. S200105ae. S200105ae was detected by LIGO and Virgo during the morning Palomar time on 2020-01-05 UT⁶. Because it was originally identified as having a FAR above the threshold for automated public release, the skymap was not released until the following day. On 6 January 2020, beginning at 02:21:59 UT (hereafter night 1), only $\sim 2\%$ of the localization was covered serendipitously by ZTF routine survey operations^{5,31–33}, which have 30 s observations, emphasizing that the delay in the skymap may have been a critical loss to the chances of detection for any fast fading counterparts.

On 7 January 2020 UT (night 2) following the belated publication of the alert by LIGO and Virgo, we adopted a survey strategy of g- and r-band exposure blocks with 180 s exposures for ZTF. The length of the exposures was chosen to balance both the depth required for a relatively distant event and the sky area requiring coverage; specifically, we optimize the exposure times to be as long as possible while covering the 90% sky area consistent with the GW event observable from Palomar and in two filters within the night. We used gwemopt^{34,35}, a codebase designed to optimize telescope scheduling for GW follow-up, to schedule the observations. The schedule is designed such that fields have reference images available to facilitate image subtraction, as well as a 30 min gap between the observations in the g- and r-bands to identify and remove moving objects. These observations were submitted from the GROWTH TOO Marshal¹⁶, which we use to ingest alerts and plan observations.

Owing to poor weather conditions at Palomar, the limiting magnitudes in the first block of night 2 were shallower than expected at a 5σ median depth of $m_{\text{AB}} = 19.5$ in the g- and r-bands (see Extended Data Fig. 1), and the second block originally scheduled for the same night was subsequently cancelled because of this³⁷. Combining the serendipitous and TOO observations, we covered 2,200 deg², corresponding to about 44% of the initial BAYESTAR and 35% of the final LALInference maps on night 2. We adopted a similar strategy on night 3 (8 January 2020 UT), and improved weather led to deeper limits, with a 5σ median depth of $m_{\text{AB}} = 20.2$ in the g- and r-bands³⁸. Combining the serendipitous and TOO observations, we covered 2,100 deg² on night 3, corresponding to about 18% of the initial BAYESTAR and 23% of the LALInference maps. In total, over the 3 nights, we covered 3,300 deg², corresponding to about 52% of the initial BAYESTAR and 48% of the LALInference maps.

S200115j. The skymap for S200115j was released during Palomar night-time on 15 January 2020 UT; we triggered TOO observations with ZTF and were on-sky within minutes. We employed the greedy-slew algorithm, same as for S200105ae, taking 300 s exposures in the g- and r-bands³⁹. Because the fields were rapidly setting by the time the skymap arrived, we were only able to cover 36% of the skymap in our TOO observations on that night. Poor weather and seeing conditions prevented us from triggering the following night (16 January 2020 UT). The subsequently released LALInference skymap shifted the innermost probability contour to the Southern lobe⁸, which was largely inaccessible to ZTF. Although we were unable to obtain further triggered observations due to poor weather, our total serendipitous and triggered coverage within three days of the merger was 1,100 deg², corresponding to about 35% probability of the initial BAYESTAR map and 22% probability of the final LALInference map.

Other teams also performed synoptic follow-up of these two events^{6,40–45}.

Candidates. For a transient event to be considered an ‘alert,’ a source extracted from a difference image must satisfy the following criteria:

1. Possess a signal-to-noise ratio ≥ 5 in positive or negative flux;
2. PSF-fit magnitude ≤ 23.5 mag;
3. The number of bad pixels in a 5×5 pixel region centred on the transient position must be ≤ 4 pixels;
4. The full-width at half-maximum of the source profile must be ≤ 7 pixels (where 1 pixel ≈ 1 arcsec);
5. The source elongation (ratio A/B of ellipse from isophotal fit) must be ≤ 1.6 ;
6. The difference between flux measurements in a fixed aperture and the PSF-fit ($\text{mag}_{\text{diff}} = \text{Aper}_{\text{mag}} - \text{PSF}_{\text{mag}}$) must fall in the range $-0.4 \leq \text{mag}_{\text{diff}} \leq 0.75$.

See ref. ³³ for alert packet contents and ref. ⁴⁶ for the ZTF alert distribution system. Hundreds of thousands of alerts are produced by ZTF every night, and the reader can find nightly alert collections in the ZTF alert archive (<https://ztf.uw.edu/alerts/public/>).

To be considered, transients must have positive residuals after image subtraction (that is, they must have brightened relative to the reference image). We require reported transients to have at least two detections separated by at least 15 min to remove potential asteroids and other moving objects. To remove contributions from likely non-transient point sources (stars in our Galaxy and distant QSOs), we remove any candidates located less than 2 arcsec from

the Pan-STARRS1 point source catalogue (PS1 PSC⁴⁷), relying on star/galaxy classification as described in ref. 48. We exclude candidates shown to be image artefacts after close inspection. We also remove any events that have detections before the trigger or are outside the 95% contour in the localization. The progression in reduction of alerts to be considered for three representative nights covering the events discussed here is shown in Extended Data Fig. 2.

For cross-validation purposes, we use three forms of candidate selection, light curve filtering and visualization tools: (1) the GROWTH Marshal⁴⁹, a web-based dynamic portal for accessing transients; (2) the Kowalski alert archive (<https://github.com/dmitrydnev/kowalski>)⁵⁰; and (3) the AMPEL alert archive (<https://github.com/AmpelProject>)^{51,52}. For our real-time human vetting involving candidates from (1), we selected candidates exhibiting interesting $g-r$ colour initially or rapid photometric evolution. Candidates retrieved via Kowalski and AMPEL (2 and 3) were all manually inspected and announced via GCN notice. As a final check, we performed a late-time Kowalski query within both event skymaps for candidates meeting the above criteria, whose forced-photometry light curves evolved faster than 0.3 mag per day and with a baseline of fewer than ten days between the first and last detection.

Observation-based NSBH constraints. In this section, we outline a methodology for converting observational upper limits to constraints on the properties of the associated KN and the merging binary. Although our upper limits lack the depth required for placing meaningful constraints on the emission from both of these NSBH mergers, and we covered less than 50% of the skymap in each case, we show that scientifically useful constraints are within reach of ZTF and similar facilities. We first illustrate how to analyse the detectability of KNe in a model-independent way using field-by-field ZTF pointings and a survey simulation software package. Then, using a new grid of KN spectra tailored to NSBH mergers, we show that observations attaining a median depth of $m_{AB} \approx 22$ mag with improved coverage could rule out certain portions of the $M_{ej,dyn}-\theta_{obs}$ parameter space, translating to constraints on the mass ratio/NS radius/BH spin. We describe our methodologies in detail below.

Model-independent constraints. We begin with a simple generic model to place the observational limits in context. For this purpose, we use *simsurvey*¹⁶, a software package initially designed and used to assess the rates of transient discovery in surveys such as ZTF by accounting for both transient and observational parameters. We adopt a toy model for transients here, injecting transients that begin at a particular absolute magnitude and decline at a certain rate measured in magnitudes per day (distributed between -1.0 mag per day and 1.0 mag per day, with negative decay rates corresponding to rising sources). We assume the transients have the same luminosity in both the g - and r -bands, and inject them in sky locations and distances consistent with the GW skymaps. Our results show that ZTF would be sensitive to rising or fading KNe brighter than $M \approx -17.5$ mag within the skymap of S200105ae, and fading KNe brighter than $M \approx -17$ mag within the skymap of S200115j. Losses in efficiency in general are due to our requirements that they are ‘detected’ at least once within the fields we observed with ZTF; for this study, we are using both TOO and serendipitous observations up to 72 h after the merger, including time- and field-dependent limiting magnitudes from those observations. We assume that the simulated transients evolve at the same rate during those 72 h. However, deeper observations of future NSBH mergers could lead to stronger statements about the minimum luminosity and maximum evolution rate of a KN associated with a given GW event. In the future, as the number of NSBH merger detections increases, *simsurvey* could be used to empirically estimate the rates and luminosity function of KNe from NSBHs⁵³. Figure 3 shows the percentage of transients that should be identified consistent with the LALInference skymaps for both events, parameterized by their peak absolute magnitude and decline rate.

Ejecta mass and binary parameter constraints. We combine g - and r -band upper limits of S200105ae and S200115j with KN models to place constraints on the possible electromagnetic counterpart to these NSBH mergers^{54–57}. We use the Monte Carlo radiative transfer code POSSIS¹⁷ and create a grid of spectra from which g - and r -band light curves can be extracted and compared with observations. In particular, we explore a two-dimensional geometry and predict light curves for eleven different viewing angles, from pole (face-on, $\cos \theta_{obs} = 1$) to equator (edge-on, $\cos \theta_{obs} = 0$).

KN models published using POSSIS have so far focused on BNS mergers; here we present a grid more tailored to NSBH mergers. We adopt a geometry similar to that in fig. 4 of ref. 15 with two distinct ejecta components: one representing the dynamical ejecta and one the post-merger ejecta. The dynamical ejecta are characterized by a mass $M_{ej,dyn}$, concentrated within an angle $\pm\phi$ about the equatorial plane, with velocities from 0.1 to 0.3 c and are lanthanide-rich in composition (see ref. 17 for more details on the adopted opacities). For simplicity, we assume a 2D geometry, where the dynamical ejecta cover an angle 2π in the azimuthal direction; we note that this is just an approximation and numerical simulations^{58,59} suggest that this component might cover only around half of the plane (that is, a crescent rather than a torus). The post-merger ejecta are modelled as a spherical component with mass $M_{ej,pm}$, extending from 0.025 to 0.1 c and with a composition intermediate between lanthanide-poor and lanthanide-rich material⁶². Below we discuss the effect of the wind composition on the derived constraints. A

density profile scaling as $\rho \propto r^{-3}$ is assumed for both components. Spectra for this new grid are made available at https://github.com/mbulla/kilonova_models.

To place constraints on the ejected material, we fix $\phi = 30^\circ$ and run a grid of 81 models with varying ejecta masses for the two components: $M_{ej,dyn}, M_{ej,pm} \in [0.01, 0.09] M_\odot$ (step size $0.01 M_\odot$). The simulated light curves show a strong dependence on the viewing angle, with increasingly fainter KNe when moving the observer from the pole ($\cos \theta_{obs} = 1$) to the equator ($\cos \theta_{obs} = 0$). In particular, orientations in the equatorial plane are on average 2–3 mag fainter in the g -band than those along the polar direction due to the blocking effect of the dynamical ejecta^{17,60}. This blocking effect may be in part a consequence of the choice of an axisymmetric outflow geometry. For a more realistic geometry of the dynamical ejecta, the post-merger ejecta would remain unobserved for some equatorial observers. 3D radiation transfer simulations with a non-axisymmetric dynamical ejecta may thus provide stronger constraints on the ejected mass for at least some equatorial observers than the 2D simulations performed here. We note that the discrepancy mentioned in ref. 60 between their light curves and those in ref. 17 is now negligible following an update of POSSIS where the temperature is no longer parameterized and uniform but rather calculated at each time and in each zone from the mean intensity of the radiation field. In addition, we adopt thermalization efficiencies ϵ_{th} from ref. 61 rather than assuming $\epsilon_{th} = 0.5$ as in ref. 17. For instance, we obtain a g -band absolute magnitude of -15.3 mag at 1 day for the model with $M_{ej,dyn} = M_{ej,pm} = 0.02 M_\odot$ viewed face-on (compare with fig. 16 of ref. 15). Extended Data Fig. 8 provides an example set of light curves in the passbands utilized in observations in this paper. The substantially brighter emission in the i - and z -bands compared with the g - and r -bands implies that better overall constraints on the KN emission are expected. To perform this check systematically, we present Extended Data Fig. 9, which demonstrates the difference in peak magnitudes between the g - and r -bands and the i - and z -bands for the models in the NSBH grid used here. The result of brighter emission in the i - and z -bands compared with the g - and r -band holds true across the parameter space, with peak z -band observations generally exceeding those for the g -band by 1 mag or more.

To demonstrate possible constraints from deeper observations, which would have been achievable under better weather conditions, we also examine constraints given by the most limiting individual pointings in each set of observations. The aim of this analysis is to guide future follow-up comparisons, showing what constraints could have been achieved if all the observations had been taken with the same depth as those in the deepest field. Compared with the median values used above, individual observations reach deeper magnitudes (see open triangles in the left and middle panels of Fig. 4). Results of this analysis are shown in Extended Data Fig. 4, where we highlight the deepest limits for each set of observations.

The left column in Extended Data Fig. 4 summarizes results for S200105ae. The top panels show g - and r -band light curves that would be ruled out if our median limits had reached the depth of our deepest observations on each night, for different distance assumptions (209, 283 and 357 Mpc from light to dark blue). We could rule out more models at closer compared with farther distances. In particular, all the models can be ruled out by the r -band upper limit at ~ 3 days, $m_r > 22.35$ mag, with no improvement found when the other observations were added. The bottom panels show what regions of the $M_{ej,dyn}-M_{ej,pm}$ parameter space are ruled out by observations for three different viewing angle ranges: $0.9 < \cos \theta_{obs} < 1$ ($0 < \theta_{obs} < 26^\circ$), $0.6 < \cos \theta_{obs} < 0.7$ ($46^\circ < \theta_{obs} < 53^\circ$) and $0 < \cos \theta_{obs} < 0.1$ ($84^\circ < \theta_{obs} < 90^\circ$). As expected, polar orientations are more constraining than the other ranges. In particular, our deepest observations could constrain the ejecta masses to $M_{ej,dyn} \leq 0.02 M_\odot$ and $M_{ej,pm} \leq 0.04 M_\odot$ for polar directions at 283 Mpc. Weaker constraints are found for orientations away from the pole, with all KNe being sufficiently faint and thus not ruled out by upper limits for an equatorial observer (bottom-left panel).

The middle column in Extended Data Fig. 4 shows the same analysis for S200115j. For S200115j, the larger distance and shallower limits lead to fewer models ruled out and thus poorer constraints in the $M_{ej,dyn}-M_{ej,pm}$ parameter space. Specifically, models are ruled out only in the optimistic case of 261 Mpc and viewing angle close to the pole. For S200115j, the most (and only) constraining observations are the limits at ~ 1 day.

We also provide updated results for S190814bv using our NSBH-specific KN model. For S190814bv, stronger constraints can be derived even for median observing depths. These constraints are also more reliable, as observations¹⁸ covered 98% of the LVC skymap. On the other hand, constraints on the parameter space of the binary are unlikely to provide information distinct from that extracted from GW observations, as the LVC already indicates that this event has 0% probability of being EM-bright. We find that all of our KN models are ruled out for polar orientations at ≤ 267 Mpc, effectively limiting the dynamical and post-merger ejecta masses to $\leq 0.01 M_\odot$. This would lead to constraints on the binary parameters shown on Extended Data Fig. 7. For higher inclinations ($46^\circ \leq \theta \leq 53^\circ$), the constraints are similar to what we just obtained for deep observations of S200105ae, with limits on the binary parameters accordingly close to those displayed on Extended Data Fig. 5.

Data availability

The data that support the plots within this paper and other findings of this study are available from the corresponding authors on reasonable request.

Code availability

The code (primarily in python) used to produce the figures is available from the corresponding authors on reasonable request.

Received: 14 April 2020; Accepted: 20 July 2020;
Published online: 14 September 2020

References

- Lattimer, J. M. & Schramm, D. N. Black-hole-neutron-star collisions. *Astrophys. J. Lett.* **192**, L145–L147 (1974).
- Li, L.-X. & Paczynski, B. Transient events from neutron star mergers. *Astrophys. J. Lett.* **507**, L59–L62 (1998).
- Coughlin, M. W. et al. Constraints on the neutron star equation of state from AT2017gfo using radiative transfer simulations. *Mon. Not. R. Astron. Soc.* **480**, 3871–3878 (2018).
- Schutz, B. F. Determining the Hubble constant from gravitational wave observations. *Nature* **323**, 310–311 (1986).
- Bellm, E. C. et al. The Zwicky Transient Facility: system overview, performance, and first results. *Publ. Astron. Soc. Pac.* **131**, 018002 (2018).
- LIGO Scientific Collaboration & Virgo Collaboration. LIGO/Virgo S200105ae: a subthreshold GW compact binary merger candidate. *GRB Coord. Netw. Circ. No.* 26640 (2020).
- LIGO Scientific Collaboration & Virgo Collaboration. LIGO/Virgo S200115j: identification of a GW compact binary merger candidate. *GRB Coord. Netw. Circ. No.* 26759 (2020).
- LIGO Scientific Collaboration & Virgo Collaboration. LIGO/Virgo S200115j: updated sky localization and source properties. *GRB Coord. Netw. Circ. No.* 26807 (2020).
- Coughlin, M. W. et al. GROWTH on S190425z: searching thousands of square degrees to identify an optical or infrared counterpart to a binary neutron star merger with the Zwicky Transient Facility and Palomar Gattini-IR. *Astrophys. J.* **885**, L19 (2019).
- LIGO Scientific Collaboration & Virgo Collaboration. LIGO/Virgo S190426c: identification of a GW compact binary merger candidate. *GRB Coord. Netw. Circ. No.* 24237 (2019).
- LIGO Scientific Collaboration & Virgo Collaboration. LIGO/Virgo S190814bv: identification of a GW compact binary merger candidate. *GRB Coord. Netw. Circ. No.* 25324 (2019).
- Coulter, D. A. et al. Swope supernova survey 2017a (SSS17a), the optical counterpart to a gravitational wave source. *Science* **358**, 1556–1558 (2017).
- Rosswog, S. et al. Detectability of compact binary merger macronovae. *Class. Quantum Gravity* **34**, 104001 (2017).
- Barbieri, C. et al. Filling the mass gap: how kilonova observations can unveil the nature of the compact object merging with the neutron star. *Astrophys. J.* **887**, L35 (2019).
- Kawaguchi, K., Shibata, M. & Tanaka, M. Diversity of kilonova light curves. *Astrophys. J.* **889**, 171 (2020).
- Feindt, U. et al. simsurvey: estimating transient discovery rates for the Zwicky Transient Facility. *J. Cosmol. Astropart. Phys.* **2019**, 005 (2019).
- Bulla, M. POSSIS: predicting spectra, light curves, and polarization for multidimensional models of supernovae and kilonovae. *Mon. Not. R. Astron. Soc.* **489**, 5037–5045 (2019).
- Andreoni, I. et al. GROWTH on S190814bv: deep synoptic limits on the optical/near-infrared counterpart to a neutron star/black hole merger. *Astrophys. J.* **890**, 131 (2020).
- Foucart, F., Hinderer, T. & Nissanke, S. Remnant baryon mass in neutron star-black hole mergers: predictions for binary neutron star mimickers and rapidly spinning black holes. *Phys. Rev. D* **98**, 081501 (2018).
- Christie, I. M. et al. The role of magnetic field geometry in the evolution of neutron star merger accretion discs. *Mon. Not. R. Astron. Soc.* **490**, 4811–4825 (2019).
- Tanaka, M., Hotokezaka, K. & Kyutoku, K. et al. Radioactively powered emission from black hole-neutron star mergers. *Astrophys. J.* **780**, 31 (2014).
- Dietrich, T. et al. New constraints on the supranuclear equation of state and the Hubble constant from nuclear physics–multi-messenger astronomy. Preprint at <http://arXiv.org/abs/2002.11355> (2020).
- Krüger, C. J. & Foucart, F. Estimates for disk and ejecta masses produced in compact binary mergers. *Phys. Rev. D* **101**, 103002 (2020).
- Vitale, S. & Chen, H.-Y. Measuring the Hubble constant with neutron star black hole mergers. *Phys. Rev. Lett.* **121**, 021303 (2018).
- Valeev, A. F. et al. LIGO/Virgo S200105ae: AT2020pp and AT2020py 10.4m GTC spectroscopy. *GRB Coord. Netw. Circ. No.* 26702 (2020).
- Castro-Tirado, A. J. et al. LIGO/Virgo S200105ae: AT2020pq, AT2020ps and AT2020pv 10.4m GTC spectroscopy. *GRB Coord. Netw. Circ. No.* 26703 (2020).
- LIGO Scientific Collaboration & Virgo Collaboration. LIGO/Virgo S200105ae: further study ongoing for GW compact binary merger candidate. *GRB Coord. Netw. Circ. No.* 26657 (2020).
- Chatterjee, D. et al. A machine learning-based source property inference for compact binary mergers. *Astrophys. J.* **896**, 54 (2020).
- Abbott, B. P. et al. GW190425: observation of a compact binary coalescence with total mass $\sim 3.4M_{\odot}$. *Astrophys. J.* **892**, L3 (2020).
- LIGO Scientific Collaboration & Virgo Collaboration. LIGO/Virgo S200105ae: updated sky localization and EM-Bright probabilities. *GRB Coord. Netw. Circ. No.* 26688 (2020).
- Graham, M. J. et al. The Zwicky Transient Facility: science objectives. *Publ. Astron. Soc. Pac.* **131**, 078001 (2019).
- Dekany, R. et al. The Zwicky Transient Facility: observing system. *Publ. Astron. Soc. Pac.* **132**, 038001 (2020).
- Masci, F. J. et al. The Zwicky Transient Facility: data processing, products, and archive. *Publ. Astron. Soc. Pac.* **131**, 018003 (2018).
- Coughlin, M. W. et al. Optimizing searches for electromagnetic counterparts of gravitational wave triggers. *Mon. Not. R. Astron. Soc.* **478**, 692–702 (2018).
- Coughlin, M. W. et al. Optimizing multi-telescope observations of gravitational-wave counterparts. *Mon. Not. R. Astron. Soc.* <https://doi.org/10.1093/mnras/stz2485> (2019).
- Coughlin, M. W. et al. 2900 square degree search for the optical counterpart of short gamma-ray burst GRB 180523b with the Zwicky Transient Facility. *Publ. Astron. Soc. Pac.* **131**, 048001 (2019).
- Anand, S. et al. LIGO/Virgo S200105ae: upper limits from the Zwicky Transient Facility. *GRB Coord. Netw. Circ. No.* 26662 (2020).
- Stein, R. et al. LIGO/Virgo S200105ae: candidates from the Zwicky Transient Facility. *GRB Coord. Netw. Circ. No.* 26673 (2020).
- Anand, S. et al. LIGO/Virgo S200115j: candidates from the Zwicky Transient Facility. *GRB Coord. Netw. Circ. No.* 26767 (2020).
- Lipunov, V. et al. LIGO/Virgo S200105ae: global master-net observations report. *GRB Coord. Netw. Circ. No.* 26646 (2020).
- Turpin, D. et al. LIGO/Virgo S200105ae: no significant candidates in TAROT-FRAM-GRANDMA observations. *GRB Coord. Netw. Circ. No.* 26687 (2020).
- Lipunov, V. et al. LIGO/Virgo S200115j: global MASTER-Net observations report. *GRB Coord. Netw. Circ. No.* 26755 (2020).
- Han, X. H., Wei, J. Y., Guillot, S., Wang, J. & Basa, S. LIGO/Virgo S200115j: no counterpart candidate in SVOM/GWAC observations. *GRB Coord. Netw. Circ. No.* 26786 (2020).
- Steehls, D. et al. LIGO/Virgo S200115j: no notable candidates in GOTO imaging. *GRB Coord. Netw. Circ. No.* 26794 (2020).
- Noysena, K. et al. LIGO/Virgo S200115j: no significant candidates in TAROT-FRAM-GRANDMA observations. *GRB Coord. Netw. Circ. No.* 26820 (2020).
- Patterson, M. T. et al. The Zwicky Transient Facility alert distribution system. *Publ. Astron. Soc. Pac.* **131**, 018001 (2018).
- Tachibana, M. A morphological classification model to identify unresolved PanSTARRS1 sources: application in the ZTF real-time pipeline. *Publ. Astron. Soc. Pac.* **130**, 128001 (2018).
- Miller, A. A. et al. Preparing for advanced LIGO: a star-galaxy separation catalog for the Palomar Transient Factory. *Astrophys. J.* **153**, 73 (2017).
- Kasliwal, M. Metal The GROWTH marshal: a dynamic science portal for time-domain astronomy. *Publ. Astron. Soc. Pac.* **131**, 038003 (2019).
- Duev, D. A. et al. Real-bogus classification for the Zwicky Transient Facility using deep learning. *Mon. Not. R. Astron. Soc.* **489**, 3582–3590 (2019).
- Nordin, J. et al. Transient processing and analysis using AMPEL: alert management, photometry, and evaluation of light curves. *Astron. Astrophys.* **631**, A147 (2019).
- Soumagnac, M. T. & Ofek, E. O. catsHTM: a tool for fast accessing and cross-matching large astronomical catalogs. *Publ. Astron. Soc. Pac.* **130**, 075002 (2018).
- Kasliwal, M. M. et al. Kilonova luminosity function constraints based on Zwicky Transient Facility searches for 13 neutron star mergers. Preprint at <http://arXiv.org/abs/2006.11306> (2020).
- Metzger, B. D. et al. Electromagnetic counterparts of compact object mergers powered by the radioactive decay of r -process nuclei. *Mon. Not. R. Astron. Soc.* **406**, 2650–2662 (2010).
- Roberts, L. F., Kasen, D., Lee, W. H. & Ramirez-Ruiz, E. Electromagnetic transients powered by nuclear decay in the tidal tails of coalescing compact binaries. *Astrophys. J. Lett.* **736**, L21 (2011).
- Rosswog, S. The multi-messenger picture of compact binary mergers. *Int. J. Mod. Phys. D* **24**, 1530012 (2015).
- Kasen, D., Metzger, B., Barnes, J., Quataert, E. & Ramirez-Ruiz, E. Origin of the heavy elements in binary neutron-star mergers from a gravitational-wave event. *Nature* **551**, 80–84 (2017).
- Kyutoku, K., Ioka, K., Okawa, H., Shibata, M. & Taniguchi, K. Dynamical mass ejection from black hole-neutron star binaries. *Phys. Rev. D* **92**, 044028 (2015).
- Foucart, F. et al. Dynamical ejecta from precessing neutron star-black hole mergers with a hot, nuclear-theory based equation of state. *Class. Quantum Gravity* **34**, 044002 (2017).

60. Kawaguchi, K., Shibata, M. & Tanaka, M. Constraint on the ejecta mass for black hole-neutron star merger event candidate S190814bv. *Astrophys. J.* **893**, 153 (2020).
61. Barnes, J., Kasen, D., Wu, M.-R. & Martínez-Pinedo, G. Radioactivity and thermalization in the ejecta of compact object mergers and their impact on kilonova light curves. *Astrophys. J.* **829**, 110 (2016).

Acknowledgements

This work was supported by the GROWTH (Global Relay of Observatories Watching Transients Happen) project funded by the National Science Foundation under PIRE grant no. 1545949. GROWTH is a collaborative project among California Institute of Technology (USA), University of Maryland College Park (USA), University of Wisconsin Milwaukee (USA), Texas Tech University (USA), San Diego State University (USA), University of Washington (USA), Los Alamos National Laboratory (USA), Tokyo Institute of Technology (Japan), National Central University (Taiwan), Indian Institute of Astrophysics (India), Indian Institute of Technology Bombay (India), Weizmann Institute of Science (Israel), The Oskar Klein Centre at Stockholm University (Sweden), Humboldt University (Germany), Liverpool John Moores University (UK) and University of Sydney (Australia). This work was based on observations obtained with the 48-inch Samuel Oschin Telescope and the 60-inch Telescope at the Palomar Observatory as part of the ZTF project. ZTF is supported by the National Science Foundation under grant no. AST-1440341 and a collaboration including Caltech, IPAC, the Weizmann Institute for Science, the Oskar Klein Center at Stockholm University, the University of Maryland, the University of Washington (UW), Deutsches Elektronen-Synchrotron and Humboldt University, Los Alamos National Laboratories, the TANGO Consortium of Taiwan, the University of Wisconsin at Milwaukee and Lawrence Berkeley National Laboratories. Operations are conducted by Caltech Optical Observatories, IPAC, and UW. The work is partly based on the observations made with the Gran Telescopio Canarias (GTC), installed in the Spanish Observatorio del Roque de los Muchachos of the Instituto de Astrofísica de Canarias, in the island of La Palma. The KPED team (M.W.C., R.G.D., D.A.D., M.F., S.R.K., E.S. and R.R.) thanks the National Science Foundation and the National Optical Astronomical Observatory for making the Kitt Peak 2.1-m telescope available. We thank the observatory staff at Kitt Peak for their efforts to assist Robo-AO KP operations. The KPED team thanks the National Science Foundation, the National Optical Astronomical Observatory, the Caltech Space Innovation Council and the Murty family for support in the building and operation of KPED. In addition, they thank the CHIMERA project for use of the Electron Multiplying CCD (EMCCD). SED Machine is based upon work supported by the National Science Foundation under grant no. 1106171. The ZTF forced-photometry service was funded under the Heising-Simons Foundation grant #12540303 (PI: Graham). M.W.C. acknowledges support from the

National Science Foundation with grant no. PHY-2010970. S.A. gratefully acknowledges support from a GROWTH PIRE grant (1545949). Part of this research was carried out at the Jet Propulsion Laboratory, California Institute of Technology, under a contract with the National Aeronautics and Space Administration. E.C.K. acknowledges support from the G.R.E.A.T. research environment and the Wenner-Gren Foundations. F.F. gratefully acknowledges support from NASA through grant 80NSSC18K0565, from the NSF through grant PHY-1806278, and from the DOE through CAREER grant DE-SC0020435.

Author contributions

S.A. and M.W.C. were the primary authors of the manuscript. M.M.K. is the PI of GROWTH and the ZTF EM-GW programme. M.B., A.S.C. and F.F. led the theory and modelling. T.A., M.A., N.G., I.A. and L.P.S. support the development of the GROWTH TOO Marshal and the associated programme. T.A., R. Stein, J.S., S.B.C., V.Z.G., A.K.H.K., H.K., E.C.K., P.M. and S.R. contributed to candidate scanning, vetting and classification. E.C.B. leads the ZTF scheduler and associated interfacing with the TOO programme. B.B. interpreted the asteroid candidates. M.D.C.-G., A.J.C.-T., Y.H., R. Sánchez-Ramírez and A.F.V. provided GTC data and associated analysis. K.D. and M.J.H. provided P200 follow-up. R.G.D., D.A.D., M.F., S.R.K., E.S. and R.R. provided KPED data. M.R. and R.W. provided SEDM data. C.F., M.J.G., R.R.L., F.J.M., P.M., M.P., P.R., B.R., D.L.S., R. Smith, M.T.S. and R.W. are ZTF builders. All authors contributed to editing the manuscript.

Competing interests

The authors declare no competing interests.

Additional information

Extended data is available for this paper at <https://doi.org/10.1038/s41550-020-1183-3>.

Supplementary information is available for this paper at <https://doi.org/10.1038/s41550-020-1183-3>.

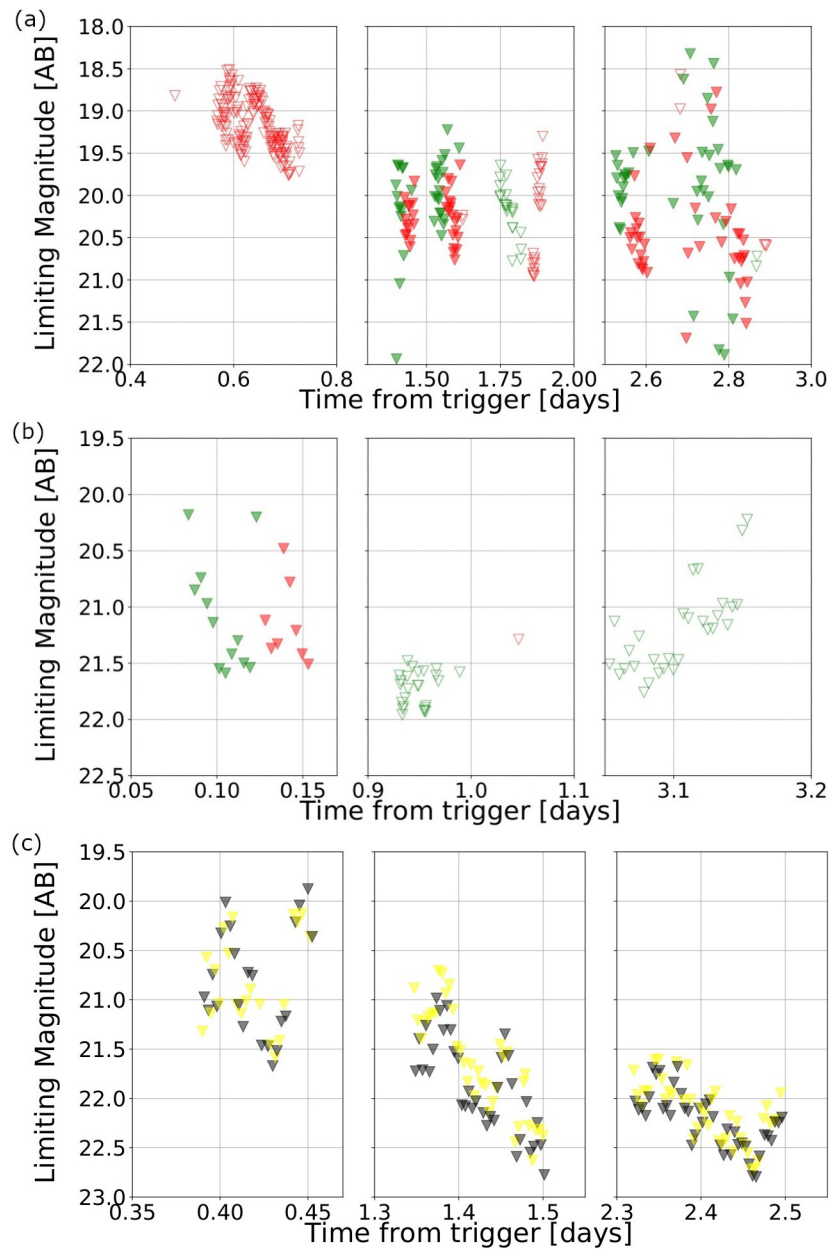
Correspondence and requests for materials should be addressed to S.A. or M.W.C.

Peer review information *Nature Astronomy* thanks Aaron Zimmerman and the other, anonymous, reviewer(s) for their contribution to the peer review of this work.

Reprints and permissions information is available at www.nature.com/reprints.

Publisher's note Springer Nature remains neutral with regard to jurisdictional claims in published maps and institutional affiliations.

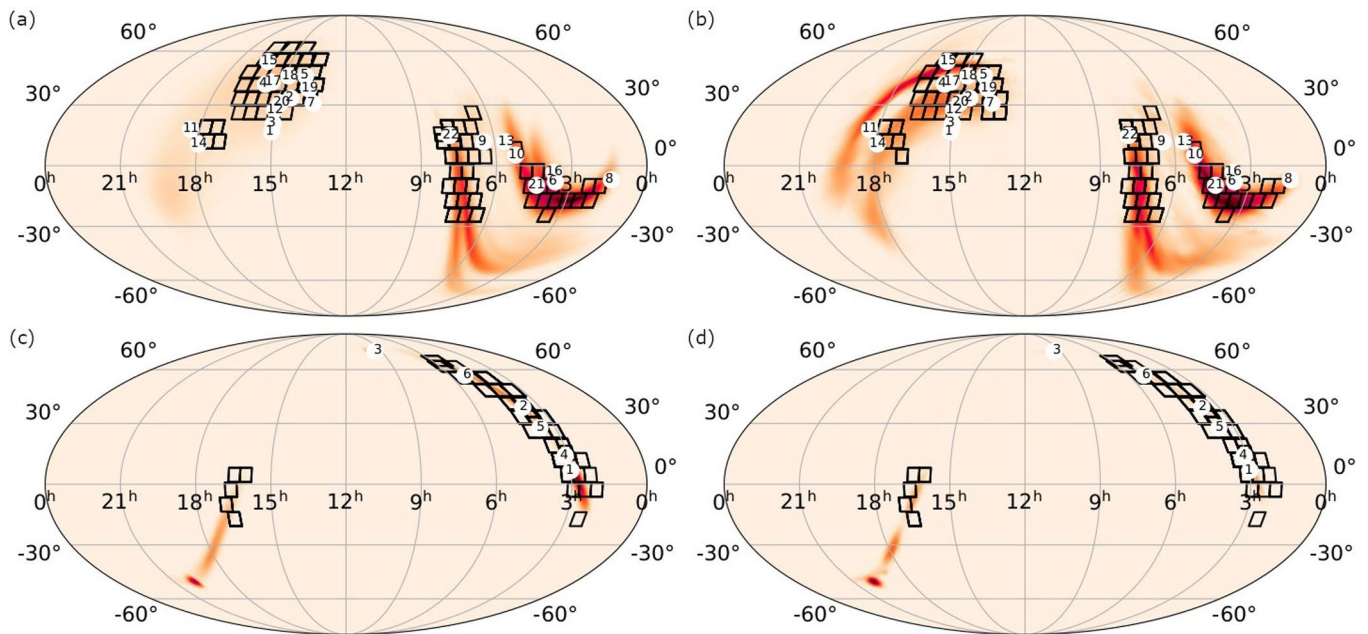
© The Author(s), under exclusive licence to Springer Nature Limited 2020



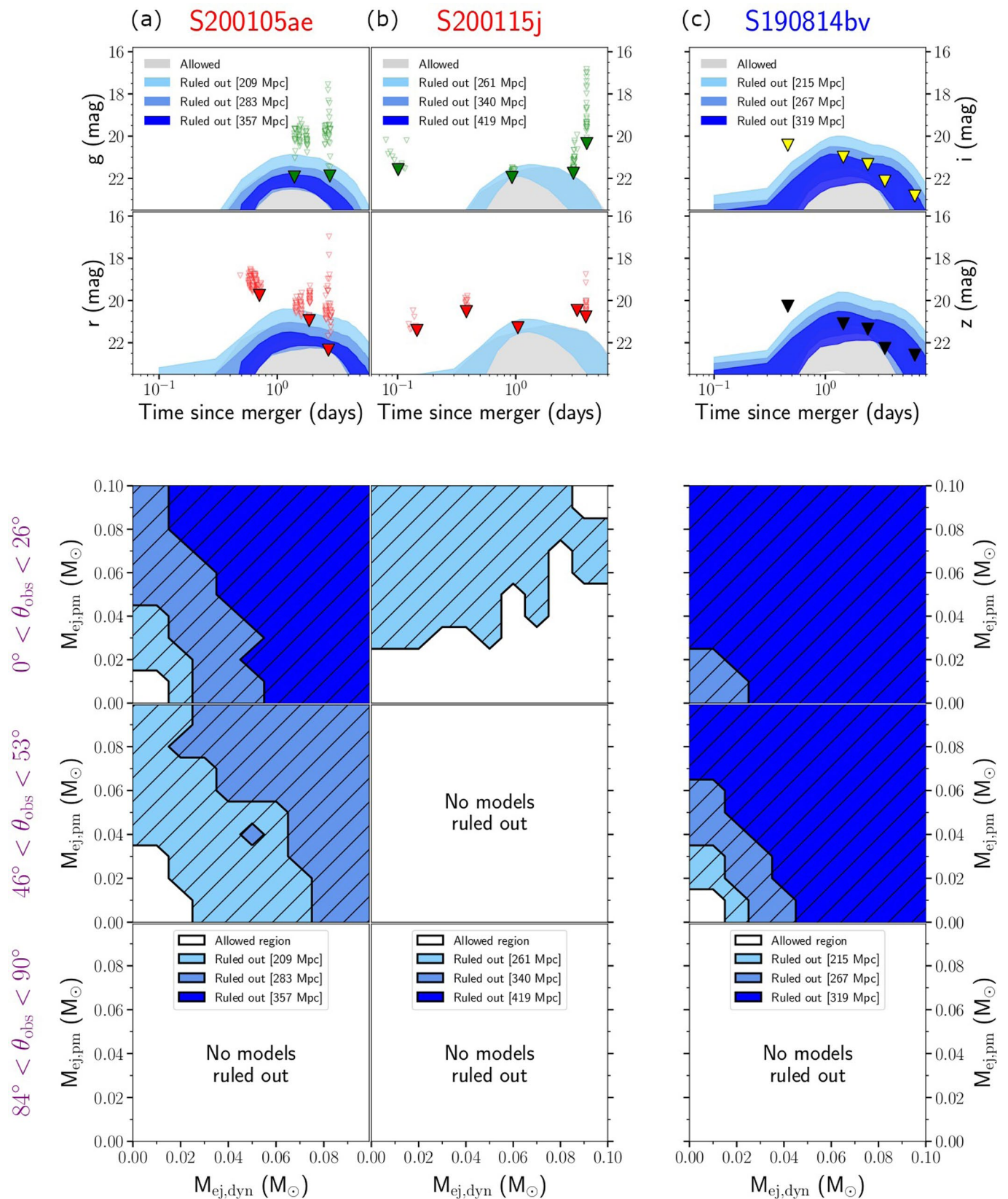
Extended Data Fig. 1 | Limiting magnitudes at each epoch of observations. $5\text{-}\sigma$ limiting magnitudes as a function of time for **a**, S200105ae (ZTF), **b**, S200115j (ZTF), and **c**, S190814bv (DECAM) with the left, middle, and right panels corresponding to observations on the first, second, and third nights for S200105ae and S190814bv and first, second, and fourth nights for S200115j. The red and green triangles correspond to the r - and g -band limits for ZTF, while the yellow and black triangles correspond to the i - and z -band limits for DECAM; the open triangles correspond to serendipitous observations and closed ToO observations. The large differences in limiting magnitude from observation to observation are due to poor weather.

Filtering criteria	# of Alerts on Jan-05	# of Alerts on Jan-06	# of Alerts on Jan-15
Alerts	313,550	205,700	48,086
Positive subtraction	246,083	139,153	36,013
Real	223,334	113,402	34,677
Not stellar	198,229	56,999	20,529
Far from a bright source	191,747	32,339	19,802
Not moving	3,439	1,916	389
No previous history	261	170	57

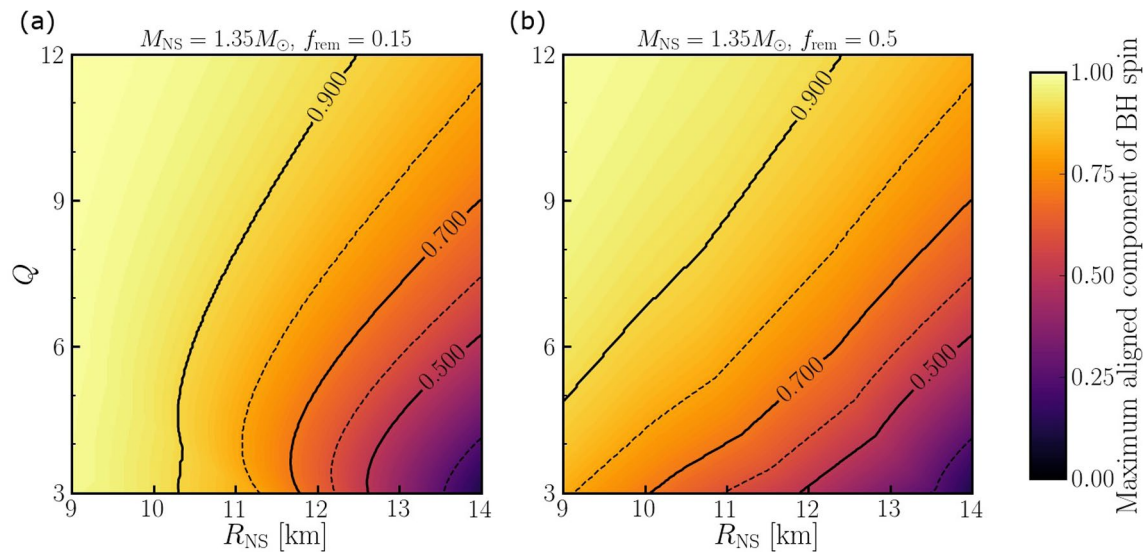
Extended Data Fig. 2 | Automatic preliminary filtering criteria for transient detection. Here we show results for each step of the ZTF filtering scheme for three representative nights covering the events discussed in this paper. Each cell shows the number of candidates that successfully pass a particular filter. The number shown is the result of running a filtering step on the alerts that met previous requirements. We define as 'Real' any alert with a real-bogus score greater than 0.25 and 'not moving' the candidates that have more than two detections separated by at least 15 minutes. The highlighted numbers represent the amount of candidates that required further vetting, as described in Section 3.



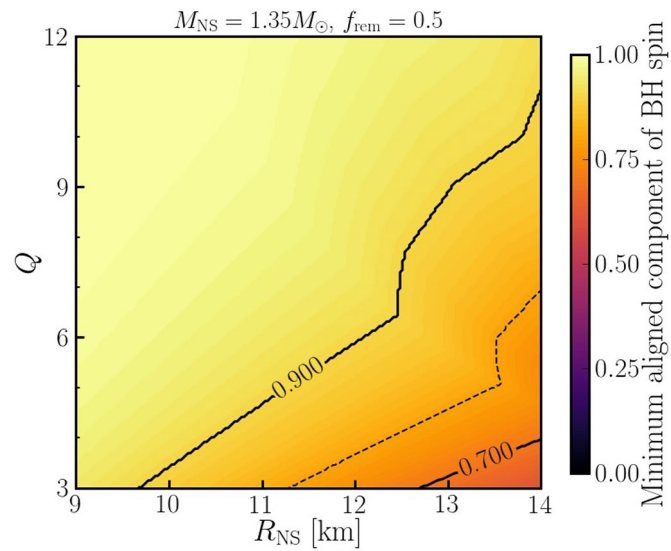
Extended Data Fig. 3 | ZTF coverage and candidates discovered within skymap. Top row: Coverage of S200105ae, showing the tiles on the 90% probability region of the initial BAYESTAR **a**, and final LALInference **b**, skymaps. The color intensity is proportional to the 2-D probability. The mapping of candidates to numbers is 1: ZTF20aaeruva, 2: ZTF20aaertpj, 3: ZTF20aaervyn, 4: ZTF20aaerqbx, 5: ZTF20aaerxsd, 6: ZTF20aafduvt, 7: ZTF20aaevbz1, 8: ZTF20aaf1ndh, 9: ZTF20aaexpwt, 10: ZTF20aafaoki, 11: ZTF20aafukgx, 12: ZTF20aagijez, 13: ZTF20aafanxk, 14: ZTF20aafujqk, 15: ZTF20aagiiik, 16: ZTF20aafdxkf, 17: ZTF20aagiipi, 18: ZTF20aagjemb, 19: ZTF20aafksha, 20: ZTF20aaertil, 21: ZTF20aafexle and 22: ZTF20aafefxe. Bottom row: Same for S200115j, with the BAYESTAR coverage shown in **c**, and LALInference coverage shown in **d**. The mapping of candidates to numbers is 1: ZTF20aagjqxg, 2: ZTF20aafqyc, 3: ZTF20aahernt, 4: ZTF20aafqpum, 5: ZTF20aafqulk, and 6: ZTF20aahakkp. We note that we include candidates up to and including within the 95% probability region, and therefore some are outside of the fields we plot here.



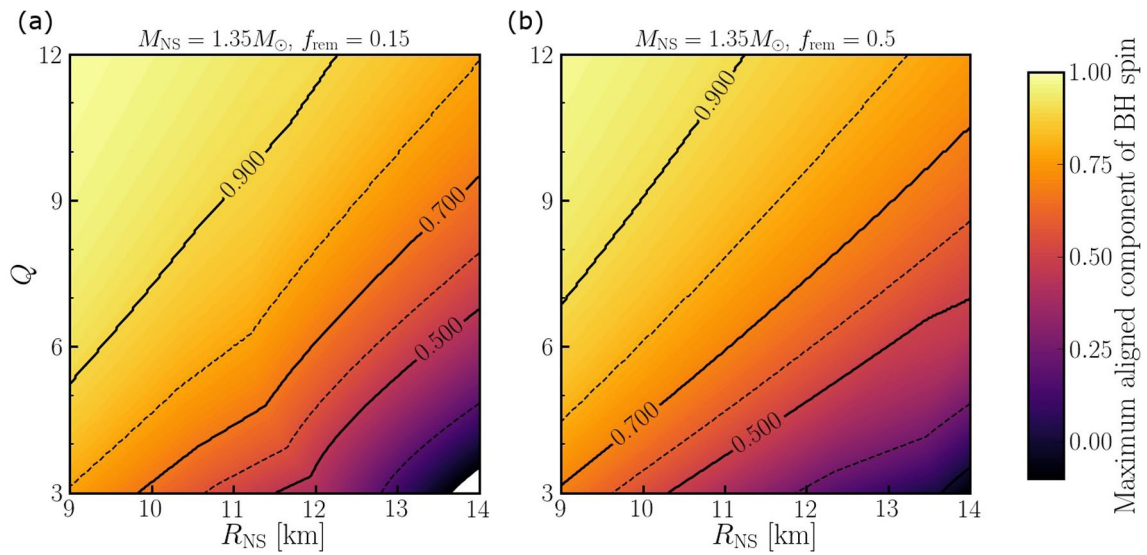
Extended Data Fig. 4 | Potential constraints on kilonova model parameters based on the deepest limiting magnitudes. We display constraints on **a**, S200105ae (ZTF), **b**, S200115j (ZTF) and **c**, S190814bv (DECam) for the models in the NSBH grid used here. Top panels: same as Figure 4 but using the deepest (filled triangles) rather than the median limits for each set of S200105ae and S200115j observations. The panel for S190814bv is the same as in Figure 4, with all limits corresponding to the median magnitudes. Bottom panels: regions of the $M_{\text{ej,dyn}} - M_{\text{ej,pm}}$ parameter space that are ruled out at different distances and for different viewing angle ranges (moving from pole to equator from top to bottom panel).



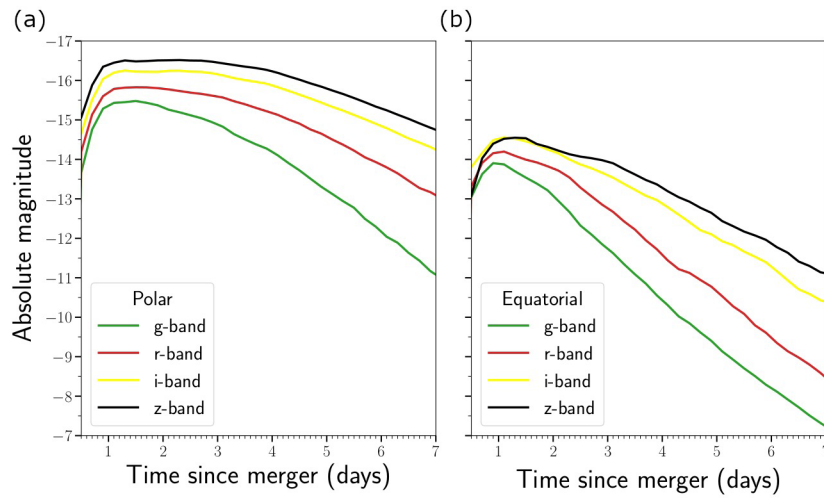
Extended Data Fig. 5 | Potential constraints on the parameters of a NSBH binary associated with S200105ae. Here we assume that $M_{\text{ej,dyn}} \leq 0.02 M_{\odot}$ and $M_{\text{ej,pm}} \leq 0.04 M_{\odot}$, appropriate for the deepest observations of S200105ae in a face-on orientation. We show the maximum value of the aligned component of the BH spin as a function of the neutron star radius R_{NS} and the binary mass ratio $Q = M_{\text{BH}}/M_{\text{NS}}$. The two panels show results assuming that low **a**, and high **b**, fractions of the post-merger accretion disk are ejected (see text). Both plots assume $M_{\text{NS}} = 1.35$. Results for different neutron star masses can be estimated from this plot simply by considering a binary with the same Q , χ and compaction $M_{\text{NS}}/R_{\text{NS}}$.



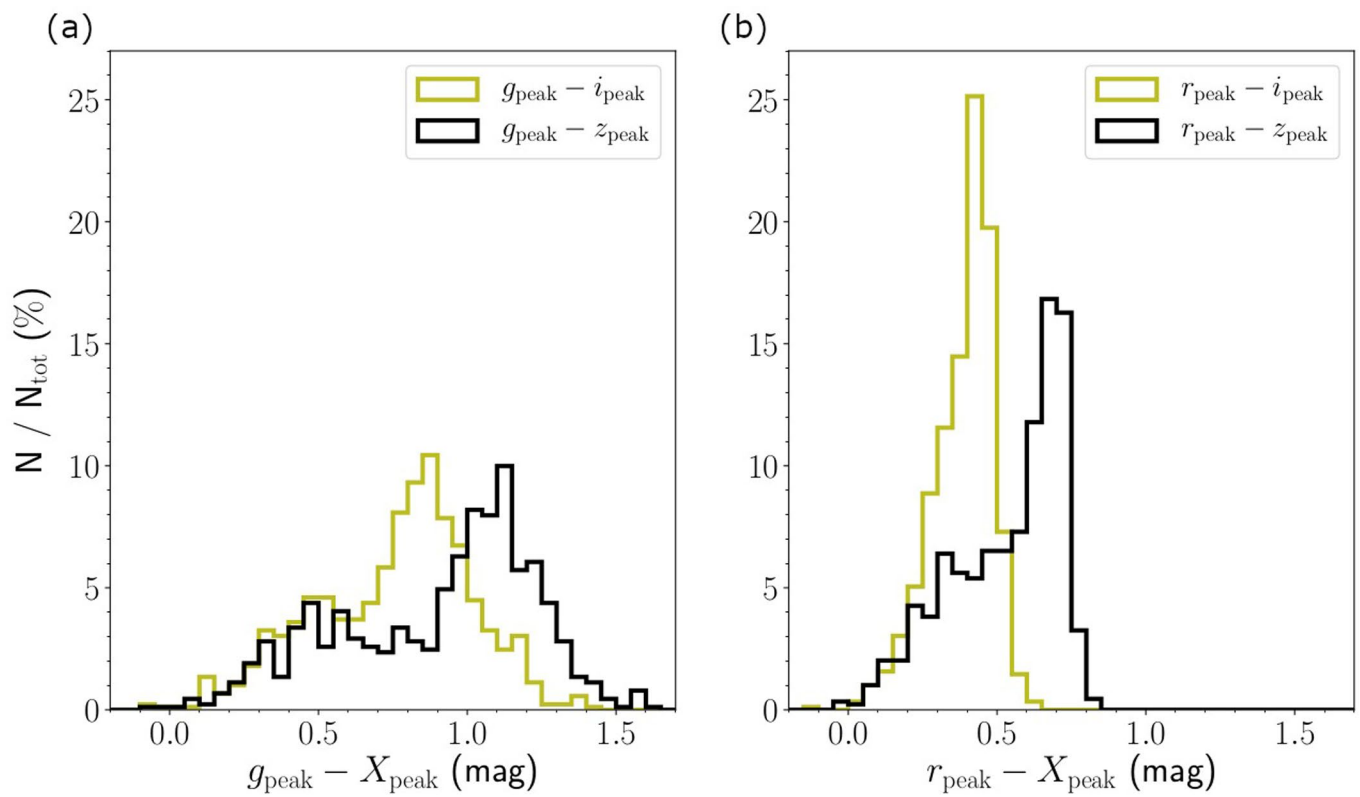
Extended Data Fig. 6 | Minimum aligned component of the BH spin above which we cannot rule out the presence of a kilonova. We cannot exclude this region of parameter space because either the resulting kilonova evolves too slowly, or the ejected mass is outside of the grid of models used in this study. In this plot, we consider the worse-case scenario of $f_{\text{rem}} = 0.5$.



Extended Data Fig. 7 | Potential constraints on the parameters of a NSBH binary associated with S190814bv. Here we assume that $M_{\text{ej,dyn}} \leq 0.01 M_{\odot}$ and $M_{\text{ej,pm}} \leq 0.01 M_{\odot}$, as appropriate for S190814bv in a face-on orientation in a similar fashion to Extended Data Figure 5 with low **a**, and high **b**, fractions of disk ejecta.



Extended Data Fig. 8 | Broadband NSBH lightcurve models from POSSIS. Light curves predicted with POSSIS (Ref. ²⁰) for a NSBH model with $M_{\text{dyn}} = 0.05M_{\odot}$ and $M_{\text{pm}} = 0.05M_{\odot}$ as seen from a polar **a**, and equatorial **b**, viewing angle.



Extended Data Fig. 9 | Comparison of peak magnitudes between optical and near-IR bands for NSBH models. We plot the difference in peak magnitudes between the **a**, g -band and the near-IR i - and z -bands for the models in the NSBH grid used here. Similarly, in **b**, we show the difference between r -band and the same near-IR bands.